Climate Dynamics (2005) 25: 265–284
DOI 10.1007/s00382-005-0035-2

K. -H. Seo · J. -K. E. Schemm · C. Jones · S. Moorthi

Forecast skill of the tropical intraseasonal oscillation in the NCEP GFS dynamical extended range forecasts

Received: 15 November 2004 / Accepted: 10 May 2005

Abstract This study examines the forecast performance of tropical intraseasonal oscillation (ISO) in recent dynamical extended range forecast (DERF) experiments conducted with the National Centers for Environmental Prediction (NCEP) Global Forecasting System (GFS) model. The present study extends earlier work by comparing prediction skill of the northern winter ISO (Madden-Julian Oscillation) between the current and earlier experiments. Prediction skill for the northern summer ISO is also investigated. Since the boreal summer ISO exhibits northward propagation as well as eastward propagation along the equator, forecast skill for both components is computed. For the 5-year period from 1 January, 1998 through 31 December, 2002, 30-day forecasts were made once a day. Compared to the previous DERF experiment, the current model has shown some improvements in forecasting the ISO during winter season so that the skillful forecasts (anomaly correlation > 0.6) for upper-level zonal wind anomaly extend from the previous shorter-than 5 days out to 7 days lead-time. A similar level of skill is seen for both northward and eastward propagation components during the summer season as in the winter case. Results also show that forecasts from extreme initial states are more skillful than those from null phases for both seasons, extending the skillful range by 3–6 days. For strong ISO convection phases, the GFS model performs better during the summer season than during the winter season. In summer forecasts, large-scale circulation and convection anomalies exhibit northward propagation during the peak phase. In contrast, the GFS model still has difficulties in sustaining ISO variability during the northern winter as in the previous DERF run. That is, the forecast does not maintain the observed eastward propagating signals associated with large-scale circulation; rather the forecast anomalies appear to be stationary at their initial location and decay with time. The NCEP Coupled Forecast System produces daily operational forecasts and its predication skill of the MJO will be reported in the future.

K. -H. Seo (✉) · J. -K. E. Schemm
RSIS/Climate Prediction Center/NCEP/NOAA, 5200 Auth Rd., Camp Springs, Maryland, 20746 USA
E-mail: kyong-hwan.seo@noaa.gov
Fax: +1-301-7638125

C. Jones
Institute for Computational Earth System Science, University of California, Santa Barbara, California, USA

S. Moorthi
Environmental Modeling Center/NCEP/NOAA, Camp Springs, Maryland, USA

1 Introduction

The intraseasonal oscillation (ISO) is one of the most prominent large-scale variabilities in the tropics and undergoes a peculiar seasonal variation, with most active oscillation during the northern winter and spring, and weaker activity during the northern summer (Slingo et al. 1999). The northern winter intraseasonal oscillation, also known as the Madden-Julian oscillation (MJO), is manifested as planetary-scale eastward propagating circulation and convection anomalies with timescales of about 30–70 days (e.g., Madden and Julian 1994; Hendon and Salby 1994, 1996). Because strong MJO convection is sustained largely over the warm pool waters in the Eastern Hemisphere, the phase speed of large-scale winds has a geographical two-regime structure. Convectively-coupled circulation in the Eastern Hemisphere propagates eastward at a rate of $\sim$5 m s^{-1}, while the phase speed over the Western Hemisphere is $\sim$10–20 m s^{-1}. The MJO system is vertically westward tilted over the western Pacific, whereas it is more vertically aligned over the Indian Ocean (Sperber 2003).

Meanwhile, the boreal summer ISO (BSISO) has a complex spatial structure and propagation pattern due to the off-equatorial thermal equator and the interaction of Asian summer monsoon (e.g., Lau and Chan 1986a; Annamalai and Slingo 2001; Hsu and Weng 2001; Kemball-Cook and Wang 2001; Lawrence and Webster 2001; Jones et al. 2004a). Intraseasonally bandpassed OLR anomalies display a northward propagating mode over the Indian Ocean and northwestward moving mode over the western Pacific Ocean as well as an eastward propagating component along the equator. Note that in this study we refer to the northern winter ISO as the MJO and the northern summer ISO as the BSISO to take into account the seasonality in the ISO.

The interaction between ISO convection and large-scale circulation anomalies influences extratropical regions. The evolution and propagation of ISO convection have been shown to develop persistent North Pacific circulation anomalies and extreme precipitation events along the western United States during boreal winter (e.g., Weickmann 1983; Liebmann and Hartmann 1984; Lau and Philips 1986b; Higgins and Schubert 1996; Mo and Higgins 1998; Jones 2000). Furthermore, the westerly wind events associated with the eastward propagation of the ISO significantly modify the thermocline structure in the equatorial Pacific Ocean via a series of downwelling oceanic Kelvin waves (McPhaden 1999, 2004). Recently, Seo and Xue (2005) show from the analysis of global ocean data assimilation systems at the National Centers for Environmental Prediction (NCEP) that the peaks of ISO-generated oceanic Kelvin wave activity lead ENSO mature phases by 5–11 months and the Kelvin wave activity also tends to impact the growth and termination of ENSO warm events. The Asian summer monsoon system is also strongly influenced by the boreal summer ISO (BSISO). The intraseasonal tropical convection variation over the Indian Ocean and the South China Sea has been found to be connected to the fluctuations of the Indian summer monsoon and the rainy spells in China (Mei-yu) (Sikka and Gadgil 1980; Lau and Chan 1986a, b; Annamalai and Slingo 2001). The active and break cycle of the monsoon is significantly related to the northward propagation of the convective anomaly from the Bay of Bengal or the Indian Ocean to the subcontinent (Krishnan et al. 2000; Annamalai and Slingo 2001). Also, the BSISO occurring in the eastern Pacific Ocean has been known to change sea surface temperature and modulate tropical cyclone activity (Maloney and Hartmann 2000; Maloney and Kiehl 2002). Indeed, there is clear evidence that a proper representation of tropical intraseasonal convective forcing helps enhance extended-range weather forecast skill in the extratropics (Ferranti et al. 1990). Therefore, it is essential to assess the ability of global climate models to forecast the variations associated with the ISO.

Recent observational and modeling studies stress the importance of air–sea interaction in the development and propagation of the ISO (Krishnamurti et al. 1988; Flatau et al. 1997; Sperber et al. 1997; Waliser et al. 1999b; Woolnough et al. 2000; Kemball-Cook and Wang 2001; Kemball-Cook et al. 2002). In Kemball-Cook et al. (2002), however, even an uncoupled simulation was able to produce an intraseasonal oscillation and thus the ISO is believed to be primarily a mode of the atmosphere. They suggest that the interaction of the ISO and ocean is not solely responsible for the existence of the ISO, even if it plays an important role in its organization and intensification. For example, the variations of sea surface temperature (SST) act to help organize "horizontal moisture convergence" (Waliser et al. 1999b), the primary forcing term for the wave-CISK (conditional instability of second kind) mechanism. Even without this, however, moisture convergence can also be systematically induced by the interaction between ISO convection and large-scale circulation.

Here we assess the prediction performance of the ISO in the NCEP operational Global Forecasting System (GFS, formerly the Medium Range Forecast or MRF) model, utilizing 30-day forecast runs performed once a day for the 5 years from 1998 to 2002. The previous operational MRF runs for the years 1987 and 1988 showed significant skill score (about 10 days) for strong MJO events based on the 200-hPa velocity potential (Chen and Alpert 1990). Lau and Chang (1992) also showed the similar range of prediction skill for the global pattern of intraseasonal variability for the winter season of 1986/87 using the upper-level velocity potential. The recent dynamical extended range forecast (DERF) experiment was performed with the 1996 NCEP reanalysis version of the MRF model for the 5-year period from 1 January, 1985 to 31 December, 1989 (Schemm et al. 1996). This DERF experiment was intended to evaluate the feasibility of operational dynamic weather prediction beyond the medium-range (i.e., about 1 week). It is found that the skillful forecasts for the wintertime MJO extend out to an average of 5–6 days at the level of anomaly correlation 0.6 with 1–3 more skillful days for an initially extreme phase of MJO events (Hendon et al. 2000; Jones et al. 2000). The present study extends the earlier work by comparing prediction skill of the northern winter ISO (MJO) in the current global model with that of the previous DERF experiment. We also examine prediction skill for the northern summer ISO (BSISO). As will be shown, the NCEP GFS model tends to produce more skillful predictions during the summer season than during the winter season, for the forecasts initialized during active convection events.

2 NCEP GFS forecast runs and analysis methods

The experiments were done with the NCEP operational GFS. GFS runs in the T126L28 resolution for

the first 7 days and in the T62L28 resolution afterwards. Note that this particular configuration is utilized for NCEP ensemble forecast system. Thirty-day forecasts were initialized each day, using the 00Z reanalysis as initial conditions for the 5-year period from January 1, 1998 through December 31, 2002. The increased horizontal resolution is an important change in this model compared to the previous DERF model, where the horizontal spectral resolution was T62 (Kalnay et al. 1996).

The current operational GFS model has undergone substantial changes since 1996. These include modification of physics package such as the inclusion of prognostic cloud water, boundary layer turbulence and convection parameterization, a modification of the evaporation formulation for convective rain, inclusion of cumulus momentum mixing, enhanced gravity wave drag, etc. The radiation schemes have also been modified. Whereas the previous shortwave radiation (SW) parameterization was developed at the Geophysical Fluid Dynamics Laboratory, using portions of the scheme from Lacis and Hansen (1974), a newer, more accurate method has been developed at NCEP, based on the work of Chou and Lee (1996). The new SW scheme incorporates climatological aerosol effects and a new surface albedo. The longwave radiation (LW) scheme developed by Fels and Schwarzkopf (1975) is also modified with a more proper treatment of radiative heating rates and LW cooling at the cloud top. More detailed information on the model can be seen at http://www.emc.ncep.noaa.gov/modelinfo.

Note that in this study, we do not intend to evaluate the effects of individual changes for the skill of the ISO. Rather, we wish to assess the overall performance of the current operational global model associated with the ISO.

Similar to the previous runs, SST was damped from its initial observed value to climatology with a 90-day e-folding time. From these forecast runs, we analyze zonal winds at 200 and 850 hPa (denoted as U200 and U850, respectively) and outgoing longwave radiation (OLR) for this study. The latter variable in the model is not as accurate as the winds since it depends on a physical parameterization, but it directly represents localized ISO-related convection anomalies.

For the forecast verification, the NCEP reanalysis (Kalnay et al. 1996) and the Advanced Very High Resolution Radiometer outgoing longwave radiation (AVHRR OLR) on the National Oceanic and Atmospheric Administration (NOAA) polar orbiting satellites (Liebmann and Smith 1996) are used for the same 5 years. Both forecast and validation data have 2.5°×2.5° spatial resolution.

Prior to calculating the anomaly correlation, we removed systematic model errors. This is accomplished by removing an annual cycle from the forecast and verification data, separately. The annual cycle for both forecast and analysis was constructed based on 4 years of data excluding the year of verification. Then, the high frequency components of the annual cycle were removed by retaining only the annual mean and first three annual harmonics. For forecast data, this procedure of obtaining an annual cycle is applied for each lead time ranging from 1 day to 30 days.

To extract intraseasonal variations associated with the ISO, we need to apply some filtering techniques. However, conventional bandpass filtering is not applicable since the forecast extent is 30 days, which is less than the time scale of the ISO. To overcome this difficulty, the beginning of the 30-day forecasts is padded with 30 days of the reanalysis and then the Murakami filter (Murakami 1979) is applied. In contrast to the conventional digital filtering technique that uses the convolution of input time series with a weighting function of the filter, the Murakami filter is a recursive filter and requires only two data points in the past. This filter converges so fast that there is almost no cutoff problem. The actual calculation is composed of two steps. At the first step, tentative output is calculated from the input data from which the mean value and linear trend are removed. Then this output is reversed in time and processed again to obtain the final output. This procedure results in a zero phase shift at all local frequencies. To test the accuracy of this filtering, bandpass filtered time series of 60 day (30 days padded to 30 day forecast) segments of observed U200 anomaly using the Murakami filter and the true bandpass filtered time series are compared. The percentage of the total mean root-mean-square error relative to the average U200 amplitude for the entire 30 day lead is below 10%.

This filter is also applied to the continuous verification data. A preliminary test shows no significant change in intraseasonal signals with an increase of padding size to ~35–50 days. However, it should be noted that this procedure tends to inflate forecast skill at short lead time (see also Jones et al. 2000). The analysis is done for the boreal extended winter season (1 November–31 April) and the boreal extended summer season (1 May–30 October).

To identify the most dominant phases of the ISO life cycle, we perform EOF analysis on intraseasonally filtered AVHRR OLR. The first two EOFs of the observed OLR anomalies together describe eastward progression of convection anomalies during the northern winter season, and eastward and northward propagation during the northern summer season. The first two EOFs account for 18% (23%) of the total variance for winter (summer, respectively) season with an approximate period of 45–48 days.

Strong ISO events are identified by selecting the dates when either of the two leading standardized principal components exceeds 1.5 standard deviations during the 5-year period (as in Hendon et al. 2000). According to the sign of the principal components, the four phases of the life cycle of the ISO are then designated as PC1+, PC2+, PC1−, and PC2− with each succeeding phase leading the preceding phase by a quarter cycle or about

12 days. Null events are defined as the cases where both leading principal components are simultaneously less than 0.5 standard deviations. Total days selected by the above criteria are 75(55), 61(64), 57(60), 77(47), 148(48) for the winter (summer, respectively) season. Composites are made based on the dates initialized for these five extreme phases and forecast skills are evaluated in terms of anomaly correlation and root-mean-square (RMS) error (although the latter will not be shown).

3 Systematic model errors and 200-hPa zonal wind propagation

The climatology of forecasts at each lead time is not likely to be identical to verification climatology. The use of verification climatology in the calculation of model anomalies at each grid point leads to systematic overestimates or underestimates of forecast anomaly values. Therefore, the mean model errors should first be removed prior to forming composites and assessing the prediction skill. Figure 1 shows 200-hPa zonal winds in the reanalysis and systematic model errors (defined as forecast minus reanalysis climatology) at several forecast lead times for winter and summer seasons. The northern wintertime mean field (Fig. 1a) shows upper-level easterlies in the tropics in the Eastern Hemisphere and over South America. Over the Pacific and Atlantic Oceans in the Western Hemisphere, westerly wind ducts associated with the Pacific and Atlantic wave guides are apparent. Mean model errors (Fig. 1b, c) represent a general weakening of the northern winter mean zonal winds in both the tropics and extratropics, resulting in weaker upper-level jets and decreased horizontal gradient of the zonal winds in the model. The westerly bias appears over the Maritime Continents at 3-day lead time. As lead time increases, model easterly winds weaker than the reanalysis, develop over the onset region of MJO convection. An easterly systematic bias develops over the eastern Pacific as in the previous experiments (Hendon et al. 2000; Jones et al. 2000).

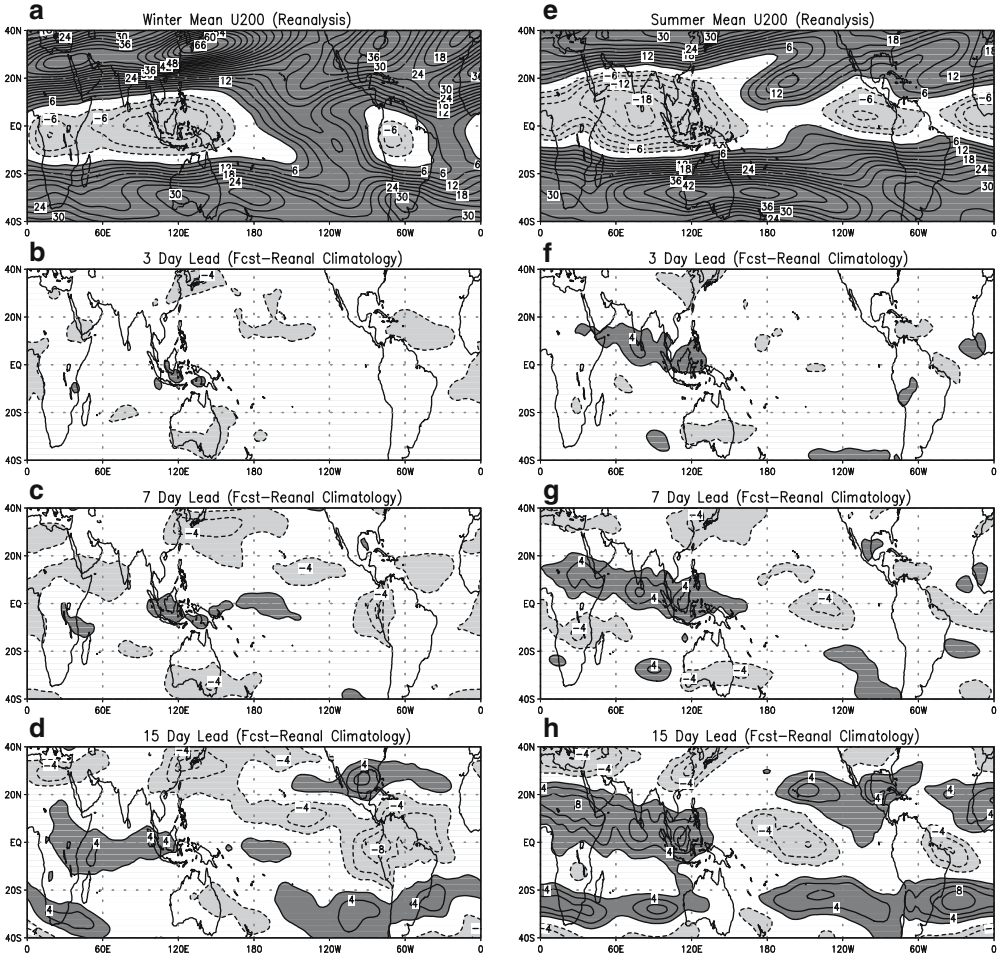

Fig. 1 **a** Mean 200-hPa zonal wind in the reanalysis (contour interval 3 m s^{-1}) and systematic model error (reanalysis minus forecast climatology) (contour interval 2 m s^{-1}) at forecast lead times of (**b**) 3, (**c**) 7, and (**d**) 15 days for the Northern Hemisphere winter season (1 November–30 April). **e** Mean 200-hPa zonal wind in the reanalysis and systematic model errors at forecast lead times of (**f**) 3, (**g**) 7, and (**h**) 15 days for the summer season (1 May–31 October). Mean model errors are calculated using unfiltered data

During the summer season (Fig. 1e), monsoonal easterlies stronger than the wintertime easterlies appear over the equatorial warm pool regions. The westerlies of the Pacific and Atlantic wave guides disappear. Over the Indian monsoon region, model easterly zonal winds are weaker than the reanalysis and this weaker dynamic response may indicate that the model has a weak representation of the monsoon heat source. As forecast time progresses, the positive model bias further intensifies and broadens.

Similarly, Figure 2 shows 850-hPa zonal winds in the reanalysis and systematic model errors at several forecast lead times for winter and summer seasons. In winter, the equatorial westerly duct appears over the main development region of the ISO. Beside that region, mean easterlies dominate in the tropics. There is no systematic downgrade or discontinuity in the forecast fields associated with the equatorial westerly duct. It has been suggested that if the low-level equatorial westerlies are weak or discontinuous, then ISO tends to show weak or discontinuous propagation (Waliser et al. 2003c). During the summer season (Fig. 2e), the dipole structure over the Indian Ocean represents the mean monsoonal low-level cross-equatorial circulation with the southeasterlies in the southern Indian Ocean and the southwesterlies in the northern Indian Ocean and south Asian

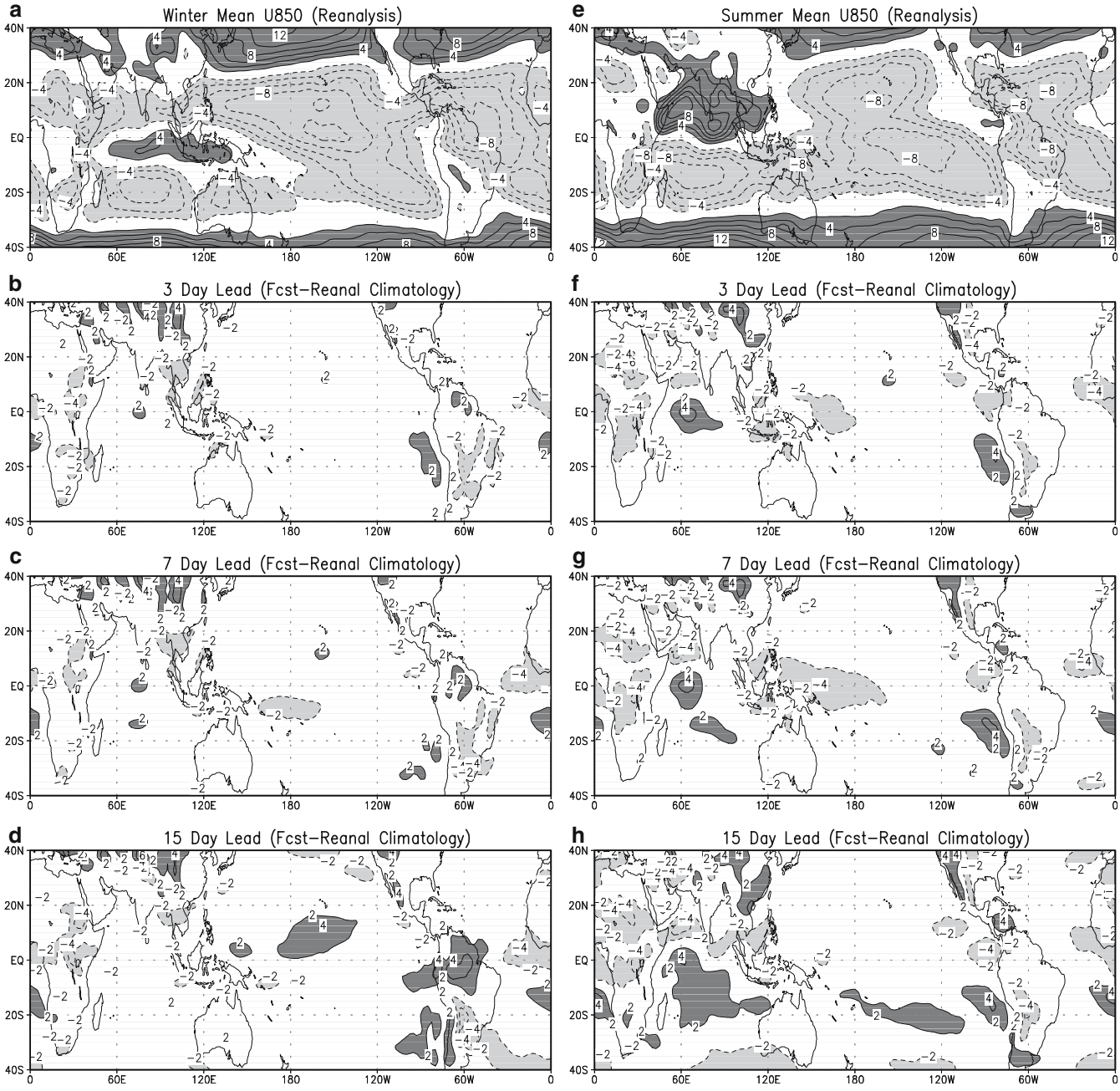

Fig. 2 Same as Fig. 1 except for mean 850-hPa zonal wind with contour interval 2 m s^{-1}

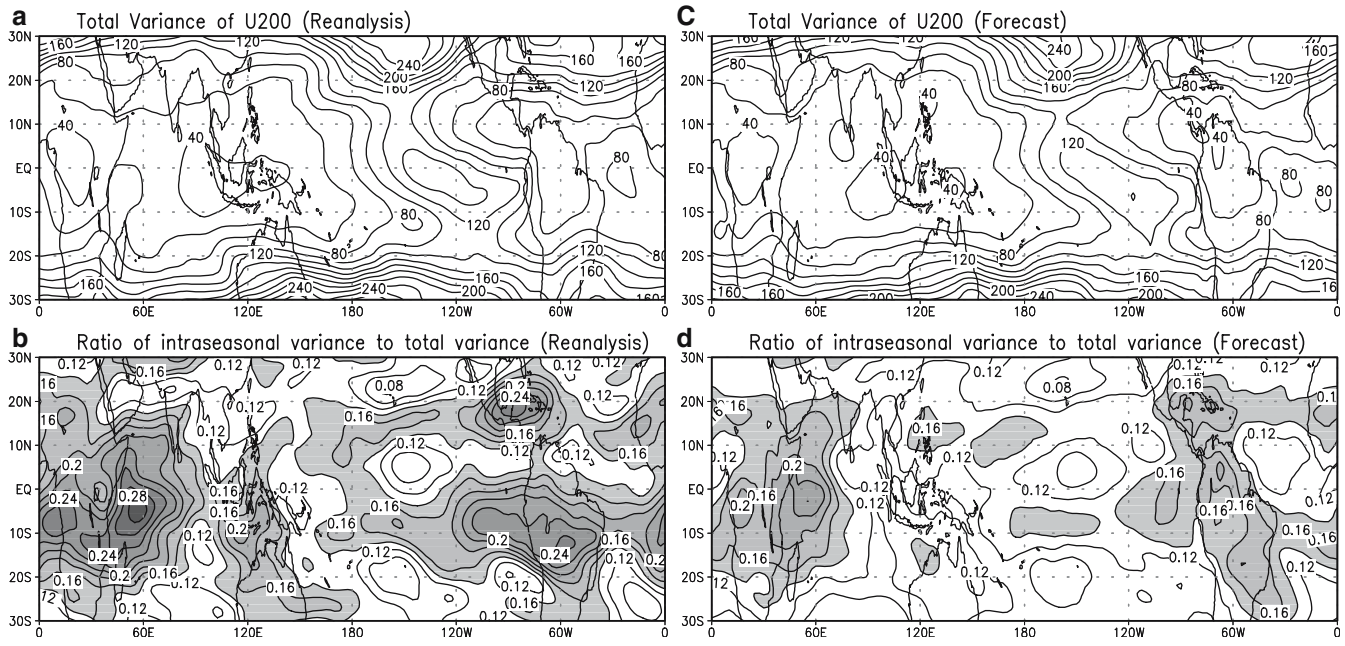

Fig. 3 **a** Total variance of unfiltered 200-hPa zonal winds in the reanalysis, and (**b**) ratio of the 30–70 day variance to the total variance for 200-hPa zonal winds for whole season. Contour intervals for total variance and ratio are 20 $m^2 s^{-2}$ and 0.02, respectively and the ratio greater than 0.14 is *shaded*. **c, d** Same as (**a**) and (**b**) except for the 3-day forecast

monsoon region. Over those regions, the forecast westerlies in the northern Indian Ocean and the forecast easterlies in the southern Indian Ocean are slightly weaker than the observations.

To assess how well the model forecasts intraseasonal variability, total variance and intraseasonally filtered variance are compared with verifying analysis. Figure 3 shows the total variance of unfiltered 200-hPa zonal winds and the ratio of the 30–70 day variance to the total variance for the reanalysis and 3-day lead forecast during the entire season. In the reanalysis, it is seen that the greatest total variance appears in relation to extratropical jets over the Pacific Ocean in both the Northern and Southern Hemispheres. In the tropics the smallest total variance is located over the Maritime Continents. However, this region shows a ratio of the bandpass-filtered variance to the total variance exceeding 14%. The western Indian Ocean is the region where the ratio attains another maximum. The two regions of higher ratio are the result of the Gill-type upper-level circulation response to the tropical diabatic forcing located over the central Indian Ocean and the western Pacific. Other large intraseasonal variance regions are situated over the subtropical continents of America.

The forecast total variance shows a horizontal pattern similar to the reanalysis with a slight difference in its intensity. The ratio of the intraseasonal variance to the total variance shows a maximum over the western Indian Ocean, but the value is smaller than in the reanalysis. In particular, the ratio over the Maritime Continents is significantly smaller than the reanalysis. This may be related to the fact that the model has a difficulty in capturing eastward-propagating intraseasonal signals, as will be shown later. Such a difficulty exited in previous studies by Hendon et al. (2000) and Jones et al. (2000). Figure 4 shows the equatorial ISO variance of 200-hPa zonal winds for all years as a function of forecast lead time. It is seen that the ISO variance decreases approximately linearly with time. The ISO variance decreases by about 20% for the lead time of 10 days. Again, this diminishing signal with forecast

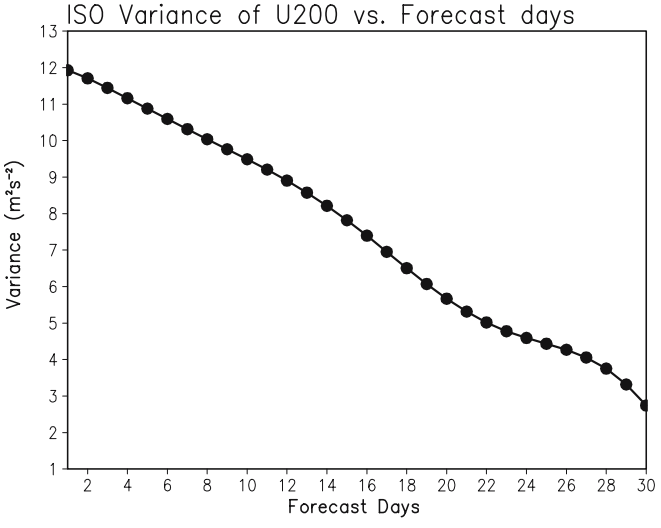

Fig. 4 Intraseasonal variance of 200-hPa zonal winds averaged over the zonal band from 30°S to 30°N as a function of forecast lead time

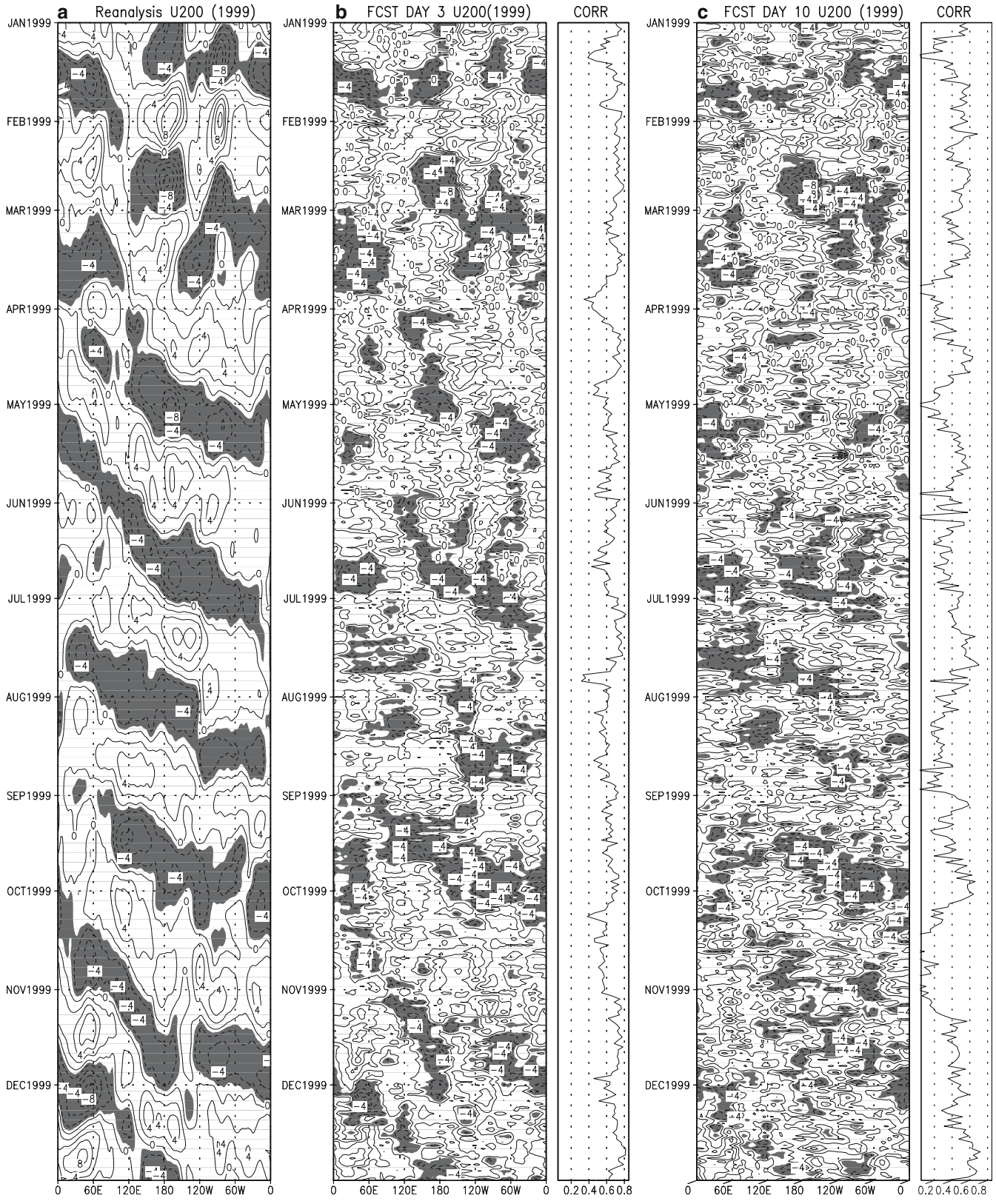

Fig. 5 Example of the propagation of the intraseasonally filtered equatorial (10°S–10°N) 200-hPa zonal wind anomalies for (**a**) the reanalysis, (**b**) and (**c**) associated 3- and 10-day forecasts and pattern correlations (*small panels*) for the year 1999. Note that the forecast data are not continuous. Anomaly values less than -2 m s^{-1} are *shaded*. Contour interval is 2 m s^{-1}

lead time indicates the decreasing forecast skill with time, which will be shown in results.

Figure 5 shows an example of the propagation of the intraseasonally filtered equatorial (5°S–5°N) upper-level zonal wind anomalies for the reanalysis and associated 3- and 10-day forecasts and pattern correlations (small panels). Since the filtering was performed on each 30-day forecast separately, the forecast data arranged according to verification dates as in the figure are discontinuous, and this introduces unavoidable high-frequency variations in the plots. Since the anomalies are taken along the equator, eastward propagating oscillation is most pronounced. Also unlike OLR anomalies, the U200 anomalies tend to appear over the whole globe. The 3-day forecast data show relatively modest resemblance to the reanalysis with an indication of stationary tendency as in the previous DERF runs (see Waliser et al. 1999a). The correlation calculated is greater than 0.5 most of the time in this case. The correct ISO signals appear to exist east of 120°E through the Western Hemisphere. This will be discussed in Fig. 10. However, the 10-day forecasts exhibit irregular patterns. Some forecasts do capture the strong ISO events such as the one in September 1999. But some do not appear to capture the strong ISO events. For example, the October 1999 event has a skill smaller than 0.2. In general, the characteristic eastward propagation is not apparent at this lead time; rather anomalies seem to move westward sometimes.

4 Prediction skill during northern winter season

4.1 Life cycle of the MJO

Before examining a phase-dependent forecast skill, composite fields of analyzed OLR and 200-hPa zonal wind anomalies associated with the ISO are presented. Applying a two-sided t test, only the fields that are statistically significant at the 95% level are considered. Figure 6 shows the composite of analyzed OLR anomalies for positive phase (PC1+ and PC2+), negative phase (PC1− and PC2−), and null cases. The PC1− and PC2− phases represent the structure similar to the PC1+ and PC2+, respectively, but the sign is opposite to the respective phases. The sequence of these plots represents a canonical life cycle of the MJO convection: initiation of the cycle over the Indian Ocean, subsequent eastward propagation of the convection in the Eastern Hemisphere, and decay of the convection in the Western Hemisphere.

Associated with this life cycle of the MJO convection, a composite of U200 anomalies and vector winds in the reanalysis for each phase is shown in Fig. 7. The distribution of upper level zonal winds shows the large-scale circulation response to the eastward moving convection, reminiscent of Gill-type spatial structure. There is an indication of Kelvin wave response, especially in the PC2 phases over the Pacific Ocean. Also, equatorial Rossby waves straddling the equator are evident, suggesting the dominance of the rotational component in zonal winds (Slingo et al. 1999). The forced Rossby waves appear to propagate further into the extratropical regions. The propagation of equatorial Kelvin-Rossby waves can be better seen in sea level pressure anomalies (not shown) as in Matthews (2000) and Seo and Kim (2003).

4.2 Prediction skill of the MJO

Figure 8a shows the anomaly correlation of U200 as a function of forecast lead time during the winter season. We define a useful skill as anomaly correlation exceeding 0.6. It is seen that the forecast skill ranges from 6 to 8 forecast days with a greater skill in the 1999/2000 and 2000/2001 winter seasons. The average skill (denoted as thick black line) is around 7 days. RMS error increases as forecast lead time increases (not shown). In Fig. 8b, the dotted line denotes the anomaly correlation for the 5-year winter mean derived by using reanalysis climatology rather than forecast climatology in the calculation of forecast anomaly. This shows only a slight difference between two approaches (i.e., with model systematic error removed and retained). However, as Inness et al. (2003) presented, the basic wind error tends to act as an impediment to the zonal propagation and fixing the basic state error in the model prior to run time allows the ISO system to prognostically generate a more realistic ISO. The dash-dotted line represents the anomaly correlation for the persistence for the entire winter season. The anomaly correlation of the persistence forecast is about 0.6 for first 5 forecast lead days, but as lead time increases, the correlation drops rapidly. The forecast skill of the MJO in the current GFS model is rather noticeably better than the 85–89 DERF experiment (dashed line).

The anomaly correlations of U200 anomalies for the different phases of the life cycle of the MJO are shown in Fig. 9. In general, extreme phases have a skill greater than the null case, as in general forecasts (see van den Dool and Toth 1991), but PC1+ and PC1− have a skill similar to or slightly smaller than the total average winter skill. Interestingly, the skill associated with PC2+ phase is greatest, indicating better upper-level wind forecasts when MJO convection is located over the Maritime Continents. Meanwhile, the enhanced convection initially located over the western or central pacific (PC1−) produces the smallest skill. The above characteristics also appeared in the earlier NCEP MRF DERF runs as in Jones et al. (1999), whereas dynamic potential predictability experiments using the National Aeronautics and Space Administration Goddard Laboratory for the Atmospheres (NASA GLA) atmospheric general circulation model by Waliser (2003a) showed opposite properties,

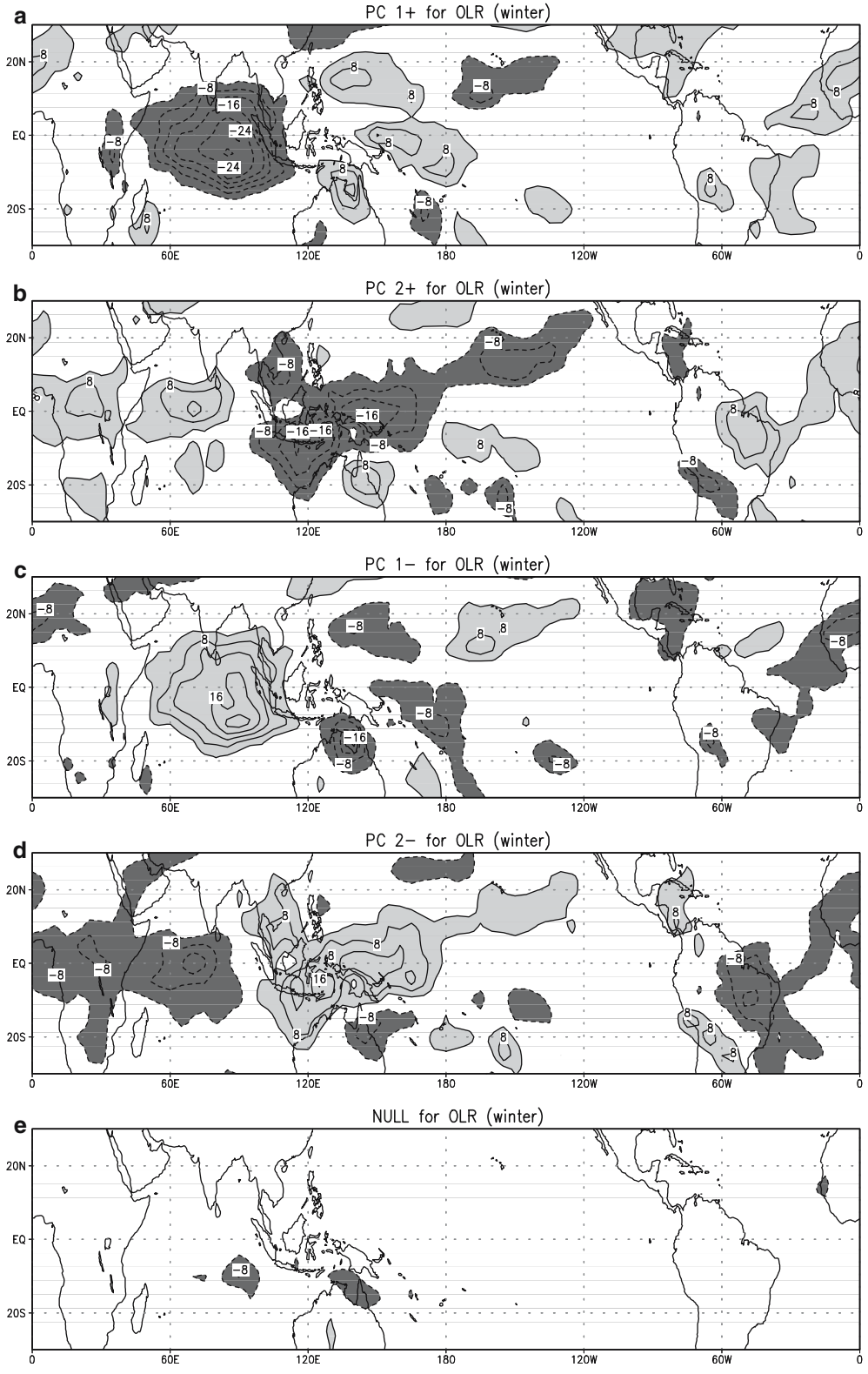

Fig. 6 Composite plots of analyzed AVHRR OLR anomalies for the phase of (**a**) PC1+, (**b**) PC2+, (**c**) PC1−, (**d**) PC2−, and (**e**) null cases during winter season. PC1+ (PC1−) denotes the events where the magnitude of the first principal component time series is greater (less) than plus (minus, respectively) 1.5 standard deviations. Similarly, PC2+ (PC2−) denotes the events where the magnitude of the second principal component time series is greater (less) than plus (minus, respectively) 1.5 standard deviations. Null cases correspond to the events where the magnitudes of both first and second coefficient time series are between 0.5 standard deviation and minus 0.5 standard deviation. Contour interval is 4 Wm^{-2}. Only statistically significant areas at the 95% level are plotted

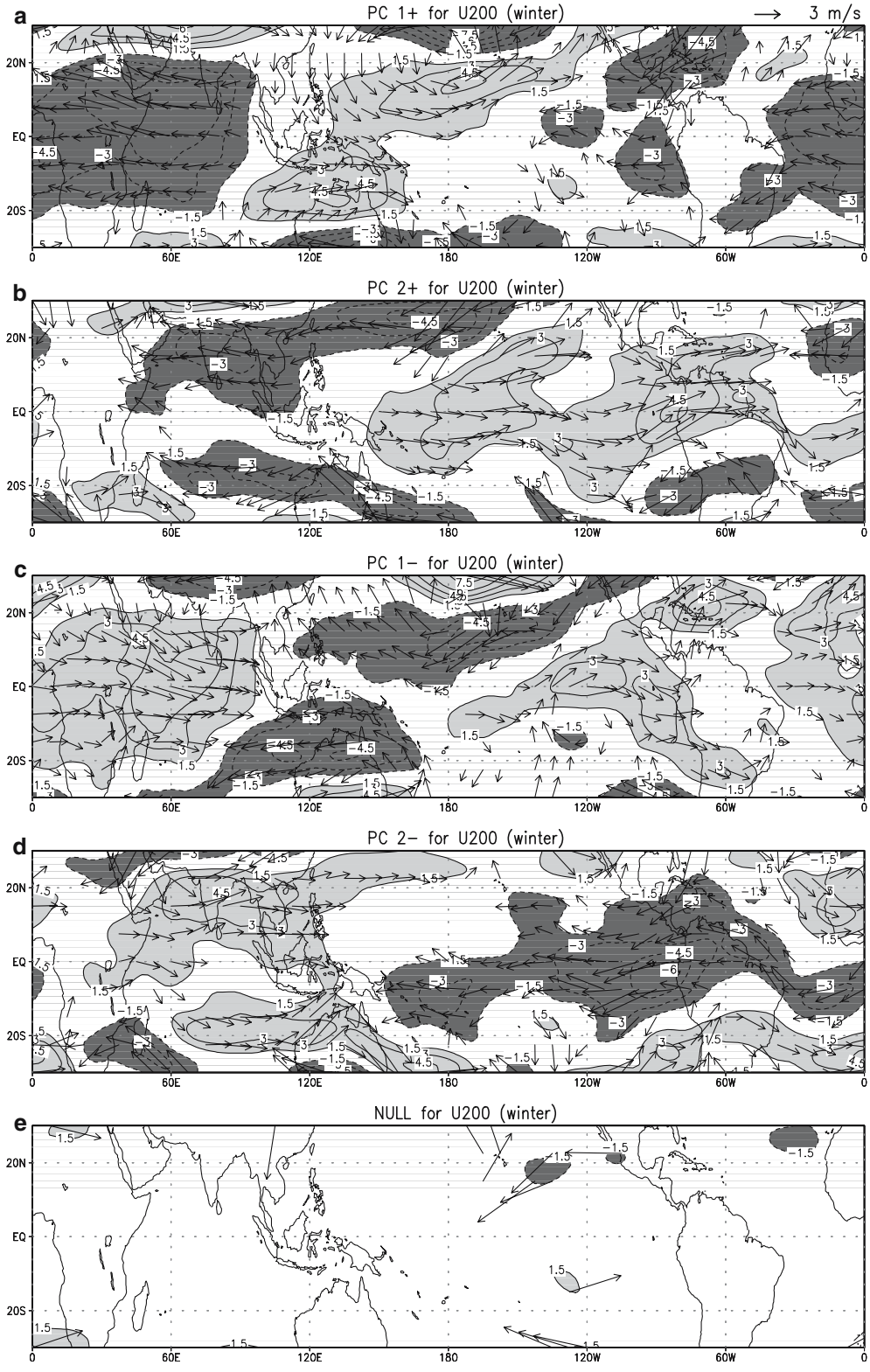

Fig. 7 Composite plots of 200-hPa zonal wind anomalies (*shaded*) and wind vector in the reanalysis for the phase of (**a**) PC1+, (**b**) PC2+, (**c**) PC1−, (**d**) PC2−, and (**e**) null cases during winter season. Contour interval is 1.5 m s^{-1}. Only statistically significant areas at the 95% level are plotted

implying that the most skillful phases are model-dependent. Figure 10 shows a longitude-time plot of anomaly correlation for each extreme phase. Typically, the downstream side of the enhanced convection (solid arrows for PC1+, PC2+ and PC1−) or suppressed convection (dashed arrow for PC2−) shows a larger

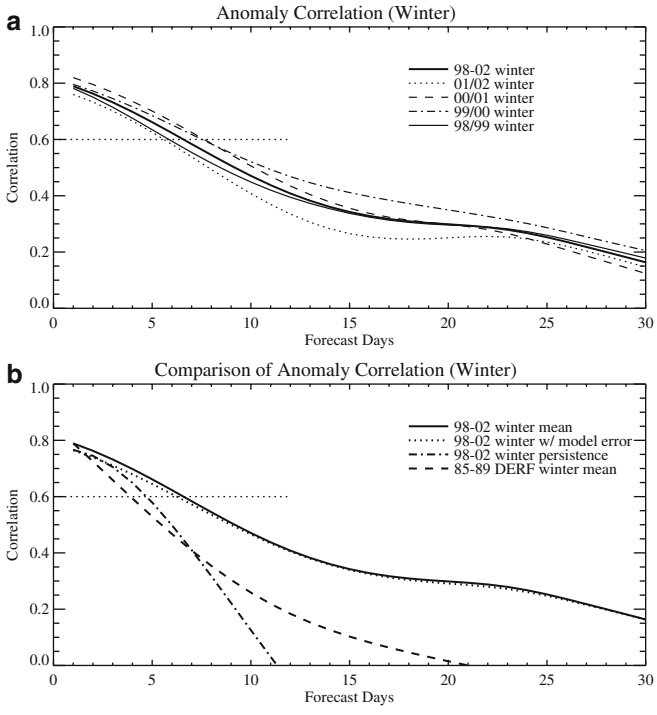

Fig. 8 **a** Anomaly correlation of U200 as a function of forecast lead time averaged over [20°S, 20°N] for individual winters (*thin lines*) and 5-year winter average (*thick line*). **b** Anomaly correlation of U200 as a function of forecast lead time averaged over [20°S, 20°N] for 5-year winter average (*thick*), the case with model error retained (*dotted*), persistence forecast (*dash-dotted*) and previous (1985–1989) dynamic extended range forecast experiments (*dashed*)

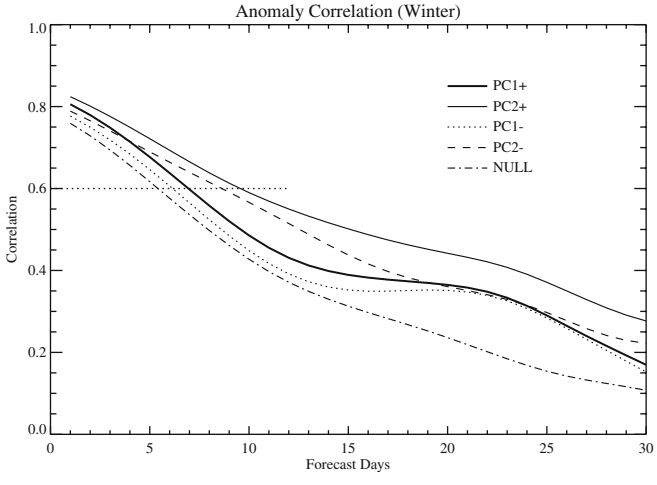

Fig. 9 Anomaly correlation of U200 as a function of forecast lead time averaged over (20°S, 20°N) for the different phases of the MJO during winter season

skill mainly from Kelvin wave response so that the higher skill tends to appear over the Pacific Ocean. The central and eastern Indian Oceans have a lower value. Another feature is a sharp drop in the correlation at the western edge of the South America. The correlation is also large over the Atlantic Ocean and Africa. It is worth mentioning that forecast skill *verified* at the time of extreme PCs is also calculated and that this approach is not significantly different from that calculated at the date *initialized* for the time of extreme PCs.

In order to compare our results with the previous DERF experiment (see Fig. 6 of Hendon et al. 2000), we plot the time evolution of 850-hPa zonal wind (U850) anomalies averaged between 5°S and 5°N for each phase, which is shown in Fig. 11. Again the five extreme phases are determined by the EOF PC of AVHRR OLR anomalies as in the previous figures. The upper panel is a composite plot of the reanalysis U850. The lower panel illustrates the composite plot of forecast U850 for the corresponding phase. It is seen that the observed wind anomalies propagate east for the four extreme phases. On the other hand, the forecast zonal wind anomalies do not tend to move to the east; instead they are mostly quasi-stationary or even move slowly westward, indicating that forecast intraseasonal variability cannot represent the eastward propagation of low-level circulation. The evolution of the forecast convection anomalies was also examined. As consistent with the propagation of the lower-level circulation, predicted OLR anomalies tend to stay at their initial location and decay rather more quickly as forecast time increases (not shown).

Anomaly correlations of U850 and OLR as a function of forecast lead times are illustrated in Figs. 12 and 13, respectively. It is seen in Fig. 12 that the average skill of U850 (thick black line) is about 5 days, which is less than the U200 case. OLR anomaly correlation shows the average skillful forecast less than 4 days (Fig. 13) with diminished lead 1 day skill by ~0.1 compared to U200 anomaly (Fig. 8b). This lowest skill in OLR compared to other variables is in agreement with the lowest estimate of potential predictability associated with anomalous convection (Waliser et al. 2003a). These diminished skills relative to that of U200 anomaly appear to arise from the fact that convection and U850 perturbations are largely confined to the Eastern Hemisphere and have a higher zonal wavenumber (Hendon and Salby 1994), whereas U200 anomaly associated with the MJO is more global in extent.

5 Prediction skill during northern summer season

5.1 Life cycle of the BSISO

The boreal summer intraseasonal oscillation (BSISO) exhibits a complex propagation pattern. Eastward propagating convection anomalies along the equator coexist with northward propagating convection anomalies from the Indian Ocean to the Indian subcontinent and northwestward moving anomalies from the western Pacific (e.g., Yasunari 1979; Krishnamurti and Subrahmanyam 1982; Wang and Xie 1997; Annamalai and Slingo 2001). This is illustrated in Fig. 14, which is the

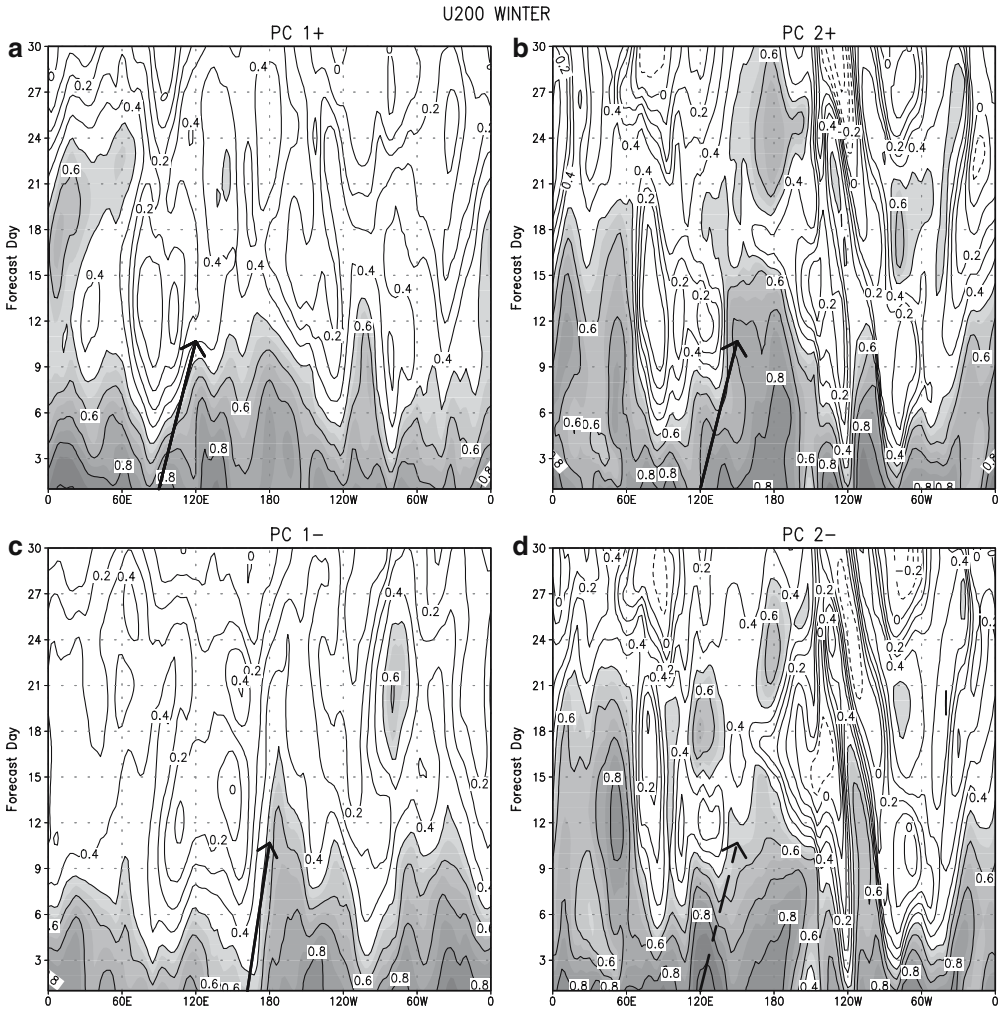

Fig. 10 Longitude-time plot of anomaly correlation of U200 for each phase during winter season. Vertical axis denotes the forecast lead time. Correlations are shown for (**a**) PC1+, (**b**) PC2+, (**c**) PC1−, and (**d**) PC2−. Anomaly correlation greater than 0.5 is *shaded*. Contour interval is 0.1. The *solid* (*dashed*) arrow represents the propagation of enhanced (suppressed) convection anomaly

composite of AVHRR OLR anomalies for each phase of the life cycle of the BSISO. Initiation of the cycle is marked by growth of the convection in the equatorial Indian Ocean (denoted as PC1+). This convection anomaly strengthens and moves eastward with time. In the Indian Ocean, the convection anomaly elongates to the north and south as Rossby waves are emitted (PC2+). The northern lobe propagates steadily northwestward, while the southern one is diminished (PC1−). A Kelvin wave response extends toward the date line. This northern lobe of the Rossby waves and the eastward moving convective anomaly from the Kelvin waves form a diagonally elongated convective band. Along with these, reduced convection of the previous cycle in the South China Sea and new reduced convection in the equatorial Indian Ocean form a quadruple-like configuration. This pattern suggests that the Indian monsoon generally exhibits an opposite phase variation with the China monsoon (Krishnan et al. 2000). The convection anomaly near the Maritime Continents, which is isolated by the eastward moving reduced convection anomaly, propagates northward (PC2−) and subsequently decays near the southern China continent (back to PC1+).

5.2 Prediction skill of the BSISO

Figure 15a shows anomaly correlation of U200 averaged over 30°–240°E and 30°S–30°N for the summer intraseasonal oscillation. The average skill is 7 days, similar to the winter case (Fig. 8a). However, the year-to-year variation of anomaly correlation is larger than the winter anomaly correlation. In Fig. 15b, like the winter case, the removal of mean model error only slightly increases the summertime forecast skill during the first 8 days and anomaly correlation by persistence forecast (dash-dotted line) drops quickly as time increases. Note that moderate variation in the above selected area for the calculation of anomaly correlation does not affect the main results.

The anomaly correlation of U200 for each phase of the BSISO is shown in Fig. 16. It is noticed that extreme phases have a prediction skill extending to more than 9 days; PC1− phase has a prediction skill extending to 12 days. PC2+ phase shows the lowest prediction skill score among four extreme phases during first 8 days. This behavior is similar to the results of potential predictability experiments performed by Waliser et al.

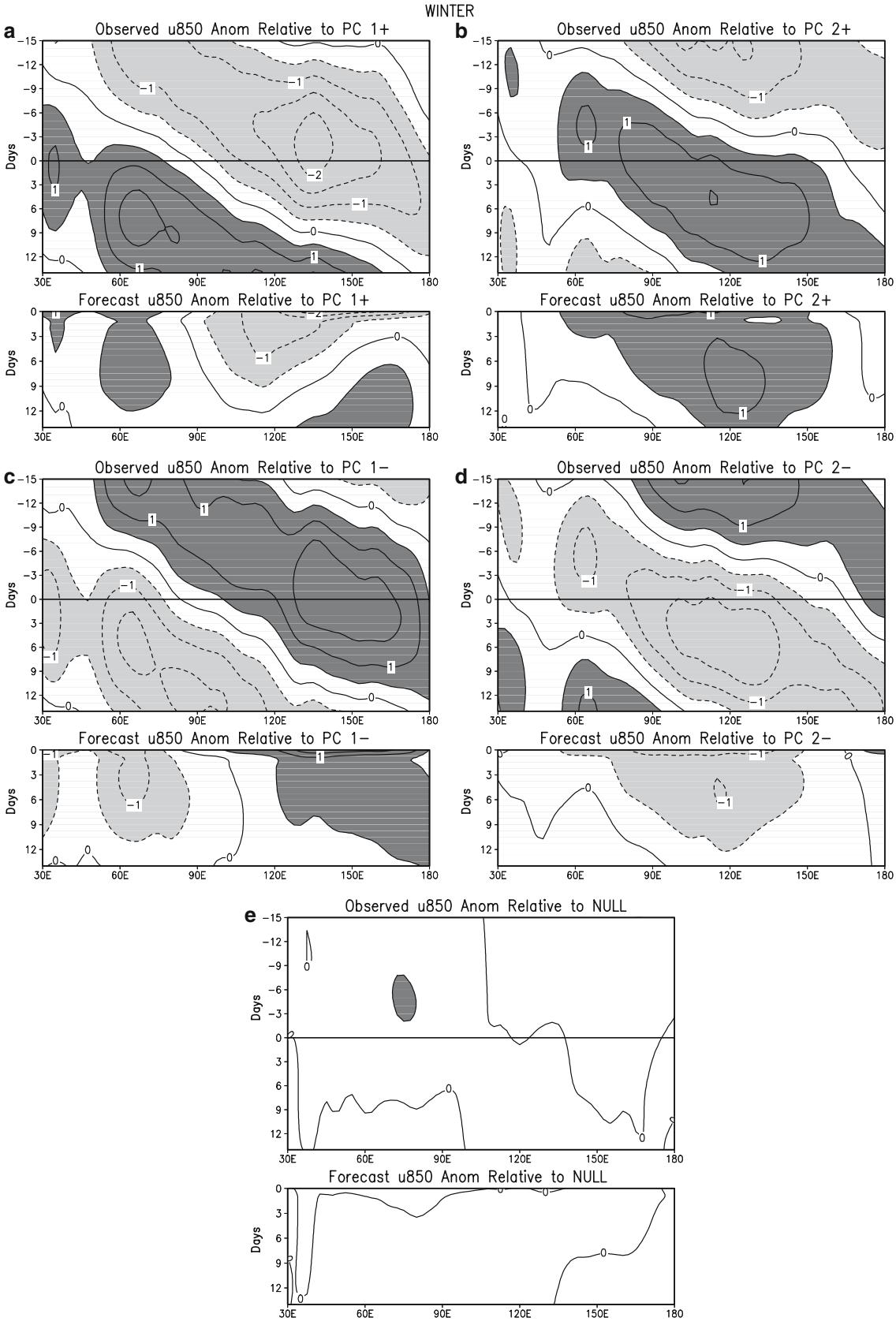

Fig. 11 Time evolution of 850-hPa zonal wind anomalies (U850) averaged between 5°S and 5°N for (**a**) PC1+, (**b**) PC2+, (**c**) PC1−, (**d**) PC2−, and (**e**) null cases for the winter season. *Upper (lower) panel* is the composite plot of the reanalysis (forecast, respectively) U850. Contour interval is 0.5 m s^{-1}. Only statistically significant fields at the 95% level are plotted

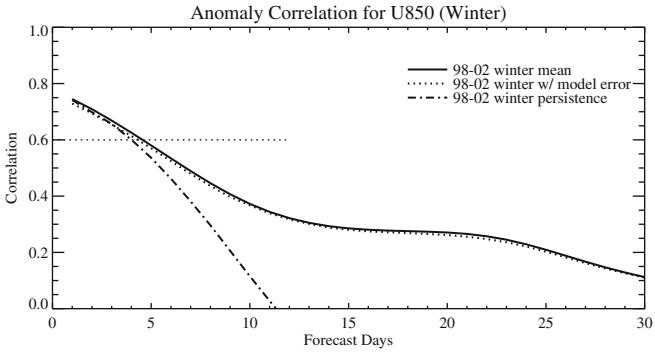

Fig. 12 Anomaly correlation of U850 as a function of forecast lead time averaged over (20°S, 20°N) in the Eastern Hemisphere for 5-year winter average (*thick*), the case with model error retained (*dotted*) and persistence forecast (*dash-dotted*)

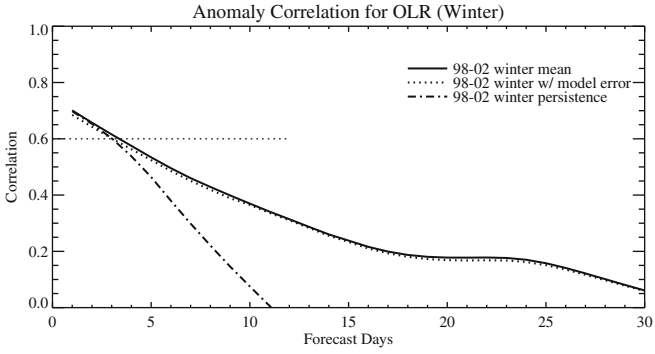

Fig. 13 Anomaly correlation of OLR as a function of forecast lead time averaged over (20°S, 20°N) in the Eastern Hemisphere for 5-year winter average (*thick*), the case with model error retained (*dotted*) and persistence forecast (*dash-dotted*)

(2003b) using the NASA GLA model. That is, their potential predictability is considerably greater for forecasts that begin when the convection anomalies are located over the Indian subcontinent, the Bay of Bengal, Indo-China peninsula, the Philippines and subtropical far-western Pacific Ocean (i.e., PC1− phase in Fig. 14), whereas it is the smallest when the convection anomalies are formed as Rossby waves over the Indian Ocean and Kelvin waves extending from the eastern Indian Ocean and Maritime region through the west Pacific (i.e., PC2+ phase in Fig. 14). On the other hand, null episodes yield a prediction skill less than 5 days since null periods are related to the weather phenomena with considerably weaker predictability. Thus, extreme episodes during the summer season provide a higher skill than their winter counterparts, whereas summertime null events produce smaller anomaly correlations than in the winter cases. Yet, it is true that extreme cases are more skillful than null events for both the seasons. It should be noted that each extreme phase takes up only 5–7% of the total summer events, so that the null plus normal cases lower the seasonal skillful days down to ~7 days (solid thick line in Fig. 15b).

Then, there is a possibility that the predicted circulation anomalies for the extreme phases really exhibit northward propagation in this season. To investigate this, latitude-time composite plots of U850 averaged between 125°E and 170°E for each phase are presented in Fig. 17. The upper and lower panels are the composite plots of the reanalysis U850 and forecast U850, respectively. The observed low-level wind anomalies propagate to the north for the four extreme phases. Indeed, the forecast zonal wind anomalies also tend to move northward even though they are rather weaker than the reanalysis. The characteristic northward propagation is also evident in the OLR anomalies (not shown). Unlike the northern winter cases, the GFS summertime forecast anomalies are seen to propagate to the north as in the observations. The BSISO also contains an eastward propagating component. Figure 18 shows time evolution of eastward propagating 850-hPa zonal wind anomalies averaged from 5°S to 5°N for extreme phases for the summer season. Interestingly, eastward propagation along the equator in summer shows a behavior very similar to the winter case (Fig. 11): the observed anomalies propagate east but forecast anomalies tend to be quasi-stationary.

Figures 19 and 20 show anomaly correlations of U850 and OLR, respectively, as a function of forecast lead times. It is seen that the average prediction skill of the northward component (thick black line) is between 5 and 6 days, which is about 1 or 2 days less than the U200 case. Anomaly correlation of the northward propagating OLR shows the average skillful forecast to be less than 5 days (Fig. 20), but this is still greater than the winter case (Fig. 13) by ~1 day. The eastward propagating component (dashed lines in Figs. 19 and 20) for U850 and OLR has a skill comparable to the northward propagating counterpart. This comparable skill can be seen in U200 anomaly (not shown). Similar to the winter case, anomalous convection has the lowest skill.

6 Summary and discussion

This study examines the prediction performance of the tropical intraseasonal oscillation in recent DERF runs conducted with the NCEP GFS model. For the 5 year period from 1 January, 1998 to 31 December, 2002, 30-day forecasts were performed once a day. The model has been updated many times since 1996, including an upgrade of radiation package, and horizontal resolution of T126 that is higher than the T62 version of the previous MRF run. The present study extends the earlier work by comparing prediction skill of the MJO in the current and previous DERF experiments. Prediction skill for the northern summer ISO has been investigated as well.

As in the previous DERF experiment, the GFS model still has difficulties in sustaining MJO variability during the northern winter. The forecast does not maintain the

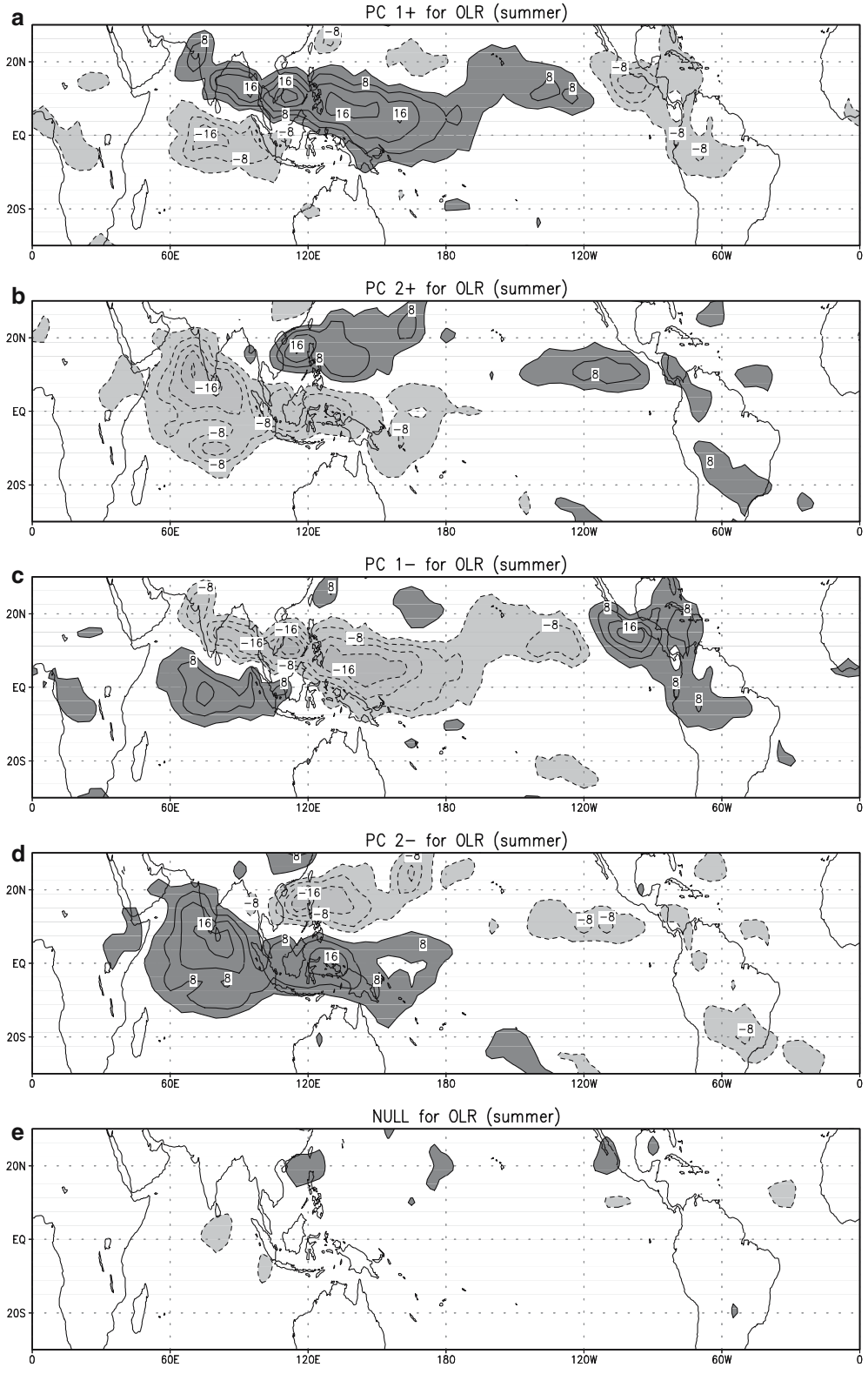

Fig. 14 Composite plots of analyzed AVHRR OLR anomalies for the phase of (**a**) PC1+, (**b**) PC2+, (**c**) PC1−, (**d**) PC2−, and (**e**) null cases during summer season. Contour interval is 4 Wm^{-2}. Only statistically significant fields at the 95% level are plotted

observed eastward propagating signals of large-scale circulation; rather the forecast anomalies seem to be stationary at their initial location and decay as time increases. However, compared to the previous experiment, the model has shown some improvements in forecasting the MJO during the winter season, such that

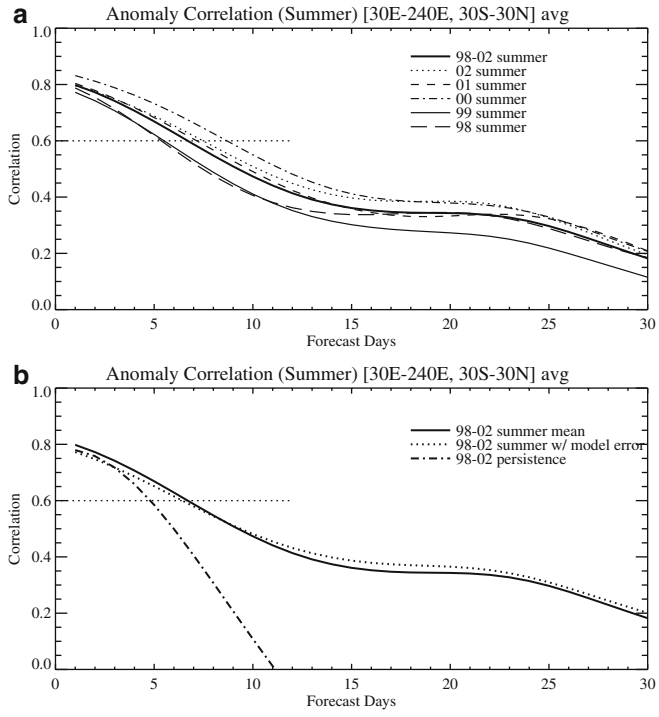

Fig. 15 **a** Anomaly correlation of U200 as a function of forecast lead time averaged over (30°–240°E, 30°S–30°N) for individual summers (*thin lines*) and 5-year summer average (*thick line*). **b** Anomaly correlation as a function of forecast lead time for 5-year summer average (*thick*), the case with model error retained (*dotted*) and persistence forecast (*dash-dotted*)

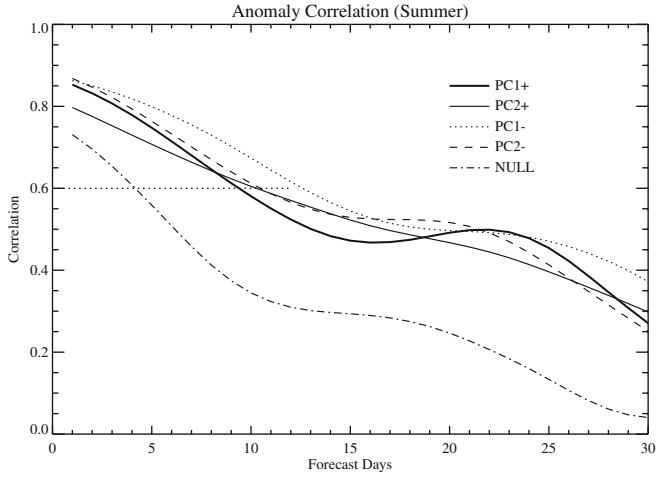

Fig. 16 Anomaly correlation of U200 as a function of forecast lead time averaged over (30°–240°E, 30°S–30°N) for the different phases of the intraseasonal oscillation during summer season

skillful forecasts (anomaly correlation > 0.6) extend out to 7 days lead-time. On average, skill level is comparable during the summer season to the winter case. The dynamical model results in forecast skill much lower than that from the statistical models by Waliser et al. (1999a), Lo and Hendon (2000) and Jones et al. (2004b) and the dynamical potential predictability experiments by Waliser et al. (2003a, 2003b). Those provide skillful forecasts in the order of 15–25 days. However, the GFS forecast is better compared to the empirical mode propagation method developed by van den Dool and Saha (2005) (see their real-time forecast in http://www.cpc.ncep.noaa.gov/products/people/wd51hd/mjo.html).

It should be mentioned that the period of the current analysis (1998–2002) is different compared to the earlier DERF runs (1985–1995). This factor may cause a difference in prediction skill mainly due to the different amplitude of intraseasonal events between the two periods. To examine this, the MJO activity index has been calculated according to the method by Slingo et al. (1999). The index is calculated as the variance of the bandpass filtered equatorial zonal mean of the U200 zonal wind (not shown). For the two DERF run periods, there is no significant difference in the MJO activity index. Therefore, the interannual variation of the MJO activity does not seem to play a critical role in the change of forecast skill of the ISO between the two specific periods.

Recently, the NCEP has performed a long-term climate simulation (referred to GFS AMIP run), in which observed SST is used as boundary forcing (not shown). Also the NCEP has coupled the GFS model with the GFDL (Geophysical Fluid Dynamics Laboratory) Modular Ocean Model version 3 (referred to Coupled Forecast System or CFS) (e.g., Wang et al. 2004). Preliminary analyses on ISO variations in these simulations show that the eastward propagation in CFS is much more evident compared to the GFS long-term climate (AMIP) run and GFS forecasts (i.e., this study). But the ISO simulated by CFS seems too strong and slow. However, the phase relationships among the winter ISO (MJO) convection, large-scale circulation and surface variables (surface fluxes and surface temperature) in CFS seem to be more consistent with observations compared to the AMIP run. For the boreal summer ISO (BSISO), CFS simulated realistic summer intraseasonal variations and meridional propagation. Also, on coupling, the phase relationships between model precipitation and various surface variables are more consistent with observations. Therefore, when SSTs are fixed or specified, model surface fluxes, surface temperature, surface moisture convergence are phased rather incorrectly relative to model convection as in previous studies by Fu and Wang (2004) and Zheng et al. (2004). Full interactive coupling between atmosphere and ocean tends to warrant correct ISO structure and dynamics. All these aspects of the GFS AMIP and CFS free runs will be documented in the near future. Additionally, 45 day data from NCEP CFS operational forecasts has been archived on a daily basis so that the ISO forecast skill can be evaluated. With this improved signal from the air–sea coupling in the CFS run, improved forecast skill of the ISO is expected.

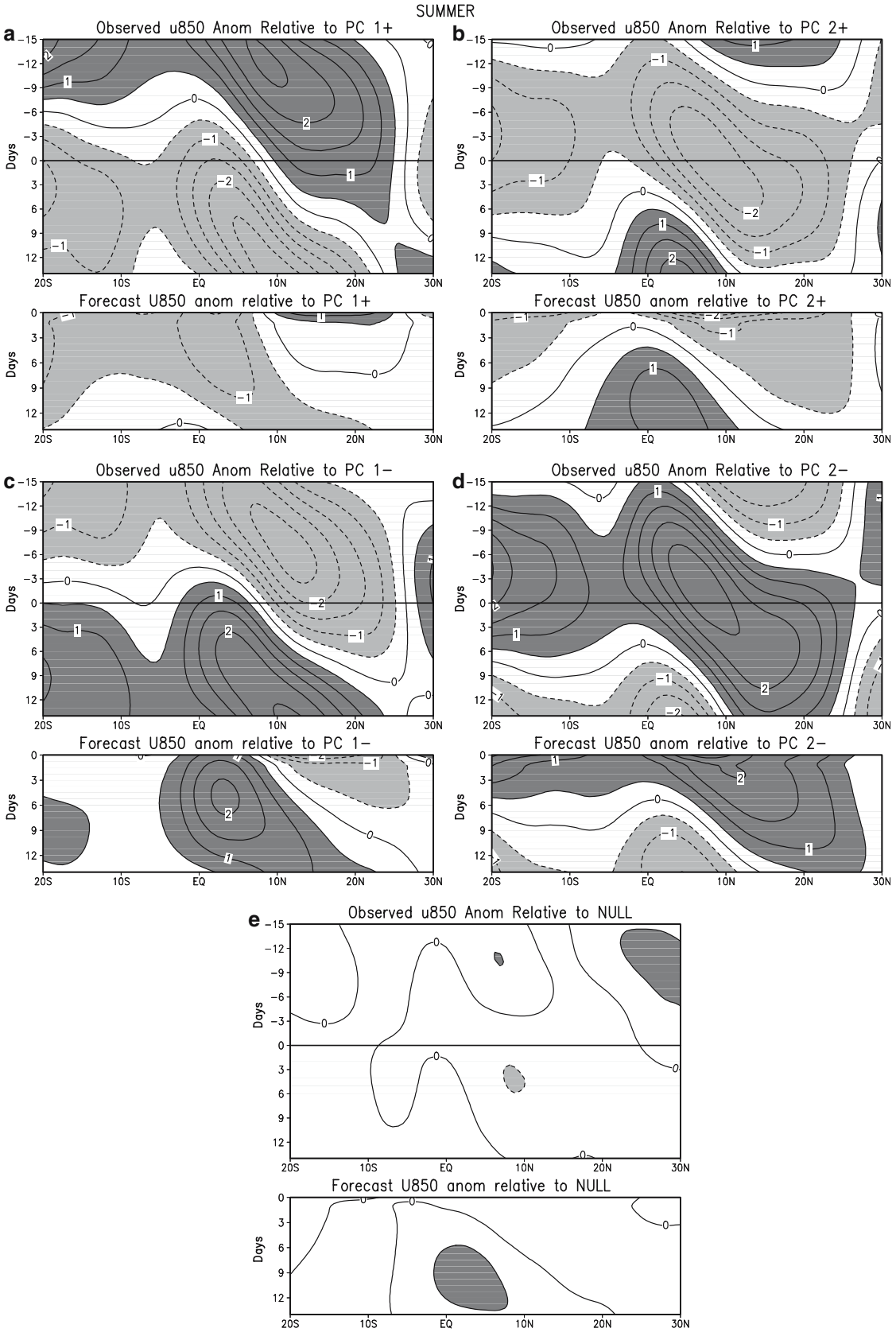

Fig. 17 Time evolution of northward propagating 850-hPa zonal wind anomalies (U850) averaged between 30°–240°E and 30°S–30°N for (**a**) PC1+, (**b**) PC2+, (**c**) PC1−, (**d**) PC2−, and (**e**) null cases for the summer season. *Upper (lower) panel* is the composite plot of the reanalysis (forecast, respectively) U850. Contour interval is 0.5 m s^{-1}. Only statistically significant fields at the 95% level are plotted

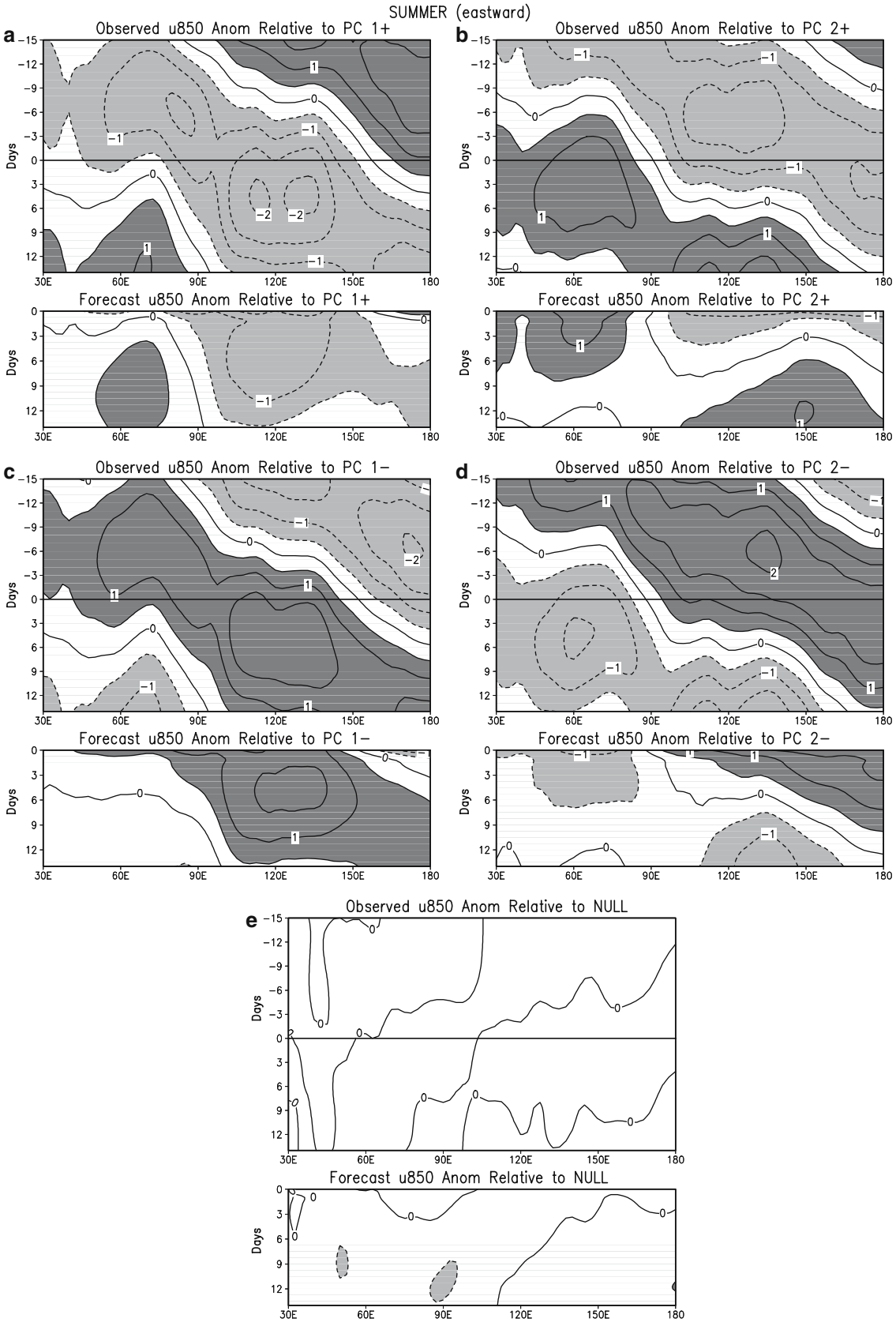

Fig. 18 Time evolution of eastward propagating 850-hPa zonal wind anomalies (U850) averaged from 5°S to 5°N for (**a**) PC1+, (**b**) PC2+, (**c**) PC1−, (**d**) PC2−, and (**e**) null cases for the summer season. *Upper (lower) panel* is the composite plot of the reanalysis (forecast, respectively) U850. Contour interval is 0.5 m s^{-1}. Only statistically significant fields at the 95% level are plotted

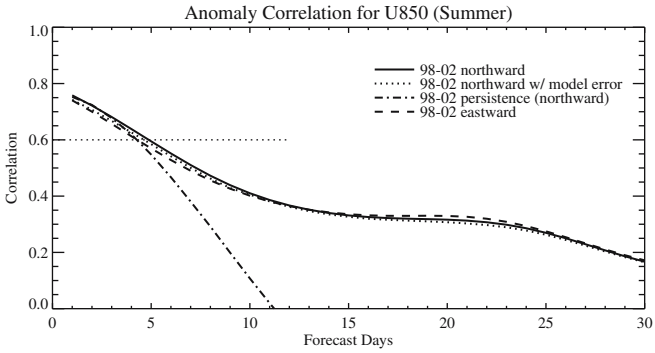

Fig. 19 Anomaly correlation of U850 as a function of forecast lead time averaged over (20°S, 20°N) in the Eastern Hemisphere for 5-year summer average (*thick*), the case with model error retained (*dotted*), persistence forecast (*dash-dotted*) for northward propagating component. Anomaly correlation for eastward propagating component along the equator is *dashed*

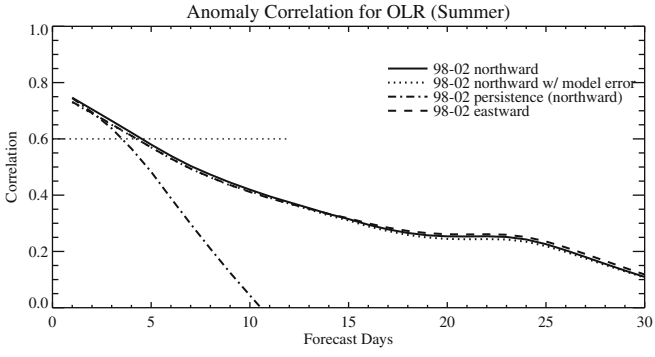

Fig. 20 Same as Fig. 19 except for OLR

Acknowledgements We would like to thank Drs. Huug van den Dool and Wanqiu Wang for their valuable comments and suggestions. We would also like to thank Drs. Ken Sperber and Duane Waliser for their careful reviews and constructive comments, which improved the manuscript. We are also grateful to Dr. Edwin Schneider for his kind proofreading. C. Jones was supported by a National Science Foundation grant (ATM-0094387).

References

Annamalai H, Slingo JM (2001) Active/break cycles: diagnosis of the intraseasonal variability of the Asian summer monsoon. Clim Dyn 18:85–102

Chen T-C, Alpert JC (1990) Systematic errors in the annual and intraseasonal variations of the planetary-scale divergence circulation in NMC medium-range forecasts. J Atmos Sci 118:2607–2623

Chou MD, Lee KT (1996) Parameterizations for the absorption of solar radiation by water vapor and ozone. J Atmos Sci 53:1203–1208

van den Dool HM, Saha S (2005) Analysis of propagating modes in the tropics in short AMIP runs. WMO to appear

van den Dool HM, Toth Z (1991) Why do forecasts for "near normal" often fail? Weather and forecasting 6:76–85

Fels SB, Schwarzkopf MD (1975) The simplified exchange approximation: a new method for radiative transfer calculations. J Atmos Sci 32:1475–1488

Ferranti L, Palmer TN, Molteni F, Klinker E (1990) Tropical-extratropical interaction associated with the 30–60 day oscillation and its impact on medium and extended range prediction. J Atmos Sci 47:2177–2199

Flatau M, Flatau PJ, Phoebus P, Niiler PP (1997) The feedback between equatorial convection and local radiative and evaporative processes: the implications for intraseasonal oscillations. J Atmos Sci 54:2373–2386

Fu X, Wang B (2004) The boreal-summer intraseasonal oscillations simulated in a hybrid coupled atmosphere-ocean model. Mon Weather Rev 132:2628–2649

Hendon HH, Salby ML (1994) The life cycle of the Madden-Julian oscillation. J Atmos Sci 51:2225–2237

Hendon HH, Salby ML (1996) Planetary-scale circulations forced by intraseasonal variations of observed convection. J Atmos Sci 51:2225–2237

Hendon HH, Liebmann B, Newmann M, Glick JD, Schemm JE (2000) Medium-range forecast errors associated with active episodes of the Madden-Julian oscillation. Mon Weather Rev 128:69–86

Higgins RW, Schubert SD (1996) Simulations of persistent North Pacific circulation anomalies and interhemispheric teleconnections. J Atmos Sci 53:188–207

Hsu H-H, Weng C-H (2001) Northwestward propagation of the intraseasonal oscillation in the Western North Pacific during the boreal summer: structure and mechanism. J Clim 14:3834–3850

Inness PM, Slingo JM, Guilyardi E, Cole J (2003) Simulation of the Madden-Julian oscillation in a coupled general circulation model. Part II: the role of the basic state. J Clim 16:365–382

Jones C (2000) Occurrence of extreme precipitation events in California and relationships with the Madden-Julian oscillation. J Clim 13:3576–3587

Jones C, Waliser DE, Schemm J-KE, Lau WKM (2000) Prediction skill of the Madden-Julian oscillation in dynamical extended range forecasts. Clim Dyn 16:273–289

Jones C, Carvalho LMV, Higgins RW, Waliser DE, Schemm J-KE (2004a) Climatology of tropical intraseasonal convective anomalies: 1979–2002. J Clim 17:523–539

Jones C, Carvalho LMV, Higgins RW, Waliser DE, Schemm J-KE (2004b) A statistical forecast model of tropical intraseasonal convective anomalies. J Clim 17:2078–2095

Kalnay E and co-authors (1996) The NCEP/NCAR 40-year reanalysis project. Bull Am Meteorol Soc 77:437–471

Kemball-Cook S, Wang B (2001) Equatorial waves and air-sea interaction in the boreal summer intraseasonal oscillation. J Clim 14:2923–2942

Kemball-Cook S, Wang B, Fu Z (2002) Simulation of the ISO in the ECHAM4 model: the impact of coupling with an ocean model. J Atmos Sci 59:1433–1453

Krishnamurti TN, Subrahmanyam D (1982) The 30–50 day mode at 850 mb during MONEX. J Atmos Sci 39:2088–2095

Krishnamurti TN, Oosterhof DK, Metha AV (1988) Air-sea interaction on the timescale of 30–50 days. J Atmos Sci 45:1304–1322

Krishnan R, Zhang C, Sugi M (2000) Dynamics of breaks in the Indian summer monsoon. J Atmos Sci 57:1354–1372

Lacis AA, Hansen JE (1974) A parameterization for the absorption of solar radiation in the Earth's atmosphere. J Atmos Sci 57:118–133

Lau K-M, Chan PH (1986a) Aspects of the 40–50 day oscillation during the northern summer as inferred from the outgoing longwave radiation. Mon Weather Rev 14:1354–1367

Lau K-M, FC Chang (1992) Tropical intraseasonal oscillation and its prediction by the NMC operational model. J Clim 5:1365–1378

Lau K-M, Phillips TJ (1986b) Coherent fluctuations of extratropical geopotential height and tropical convection in intraseasonal time scales. J Atmos Sci 43:1164–1181

Lawrence DM, Webster PJ (2001) Interannual variations of the intraseasonal oscillation in the South Asian summer monsoon region. J Clim 14:2910–2922

Liebmann B, Hartmann DL (1984) An observational study of tropical midlatitude interaction on intraseasonal time scales during winter. J Atmos Sci 41:3333–3350

Liebmann B, Smith CA (1996) Description of a complete (interpolated) OLR dataset. Bull Am Meteorol Soc 77:1275–1277

Lo F, Hendon HH (2000) Empirical extended-range prediction of the Madden-Julian oscillation. Mon Weather Rev 128:2528–2543

Madden RA, Julian PR (1994) Observations of the 40–50-day tropical oscillation – a review. Mon Weather Rev 122:814–837

Maloney ED, Hartmann DL (2000) Modulation of eastern north Pacific hurricanes by Madden-Julian oscillation. J Clim 13:1451–1460

Maloney ED, Kiehl JT (2002) MJO-related SST variations over the tropical eastern Pacific during Northern Hemisphere summer. J Clim 15:675–689

Matthews AJ (2000) Propagation mechanisms for Madden-Julian oscillation. QJR Meteorol Soc 126:2637–2651

McPhaden MJ (1999) Genesis and evolution of the 1997–98 El Niño. Science 283:950–954

McPhaden MJ (2004) Evolution of the 2002/03 El Niño. Bull Am Meteorol Soc 85:677–695

Mo KC, Higgins RW (1998) Tropical influences on California precipitation. J Clim 11:412–430

Murakami M (1979) Large-scale aspects of deep convective activity over the GATE area. Mon Weather Rev 107:994–1013

Schemm J-KE, van den Dool H, Saha S (1996) A multi-year DERF experiment at NCEP. 11th Conference on numerical weather prediction, August 19–23, 1996, Norfolk, Virginia, pp 47–49

Seo K-H, Kim K-Y (2003) Propagation and initiation mechanisms of the Madden-Julian oscillation. J Geophys Res 108(D13), 4384, doi:10.1029/2002JD002876

Seo K-H, Xue Y (2005) MJO-related oceanic Kelvin waves and the ENSO cycle: a study with the NCEP global ocean data assimilation system. Geophys Res Lett 32, L07712, doi:10.1029/2005GL022511

Sikka DR, Gadgil S (1980) On the maximum cloud zone and the ITCZ over Indian longitudes during the south west monsoon. Mon Weather Rev 108:1840–1853

Slingo JM, Powell DP, Sperber KR, Nortley F (1999) On the predictability of the interannual behaviour of the Madden-Julian oscillation and its relationship with El Niño. QJR Meteorol Soc 125:583–609

Sperber KR (2003) Propagation and veritical structure of the Madden-Julian oscillation. Mon Weather Rev 131:3018–3037

Sperber KR, Slingo JM, Inness PM, Lau K-M (1997) On the maintenance and initiation of the intraseasonal oscillation in the NCEP/NCAR reanalysis and in the GLA and UKMO AMIP simulations. Clim Dyn 13:769–795

Waliser DE, Jones C, Schemm J-KE, Graham NE (1999a) A statistical extended-range tropical forecast model based on the slow evolution of the Madden-Julian oscillation. J Clim 12:1918–1939

Waliser DE, Lau K-M, Kim J-H (1999b) The influence of coupled sea surface temperatures on the Madden-Julian oscillation: a model perturbation experiment. J Atmos Sci 56:333–358

Waliser DE, Lau K-M, Stern W, Jones C (2003a) Potential predictability of the Madden-Julian oscillation. Bull Am Meteorol Soc 84:33–50

Waliser DE, Stern W, Schubert S, Lau K-M (2003b) Dynamic predictability of intraseasonal variability associated with the Asian summer monsoon. QJR Meteorol Soc 129:2897–2925

Waliser DE, Schubert SD, Kumar A, Weickmann KL, Dole R (2003c) Modeling, simulation, and forecasting of subseasonal variability. Technical report series on global modeling and data assimilation, NASA/CP-2003–104606, 25, p 65

Wang B, Xie X (1997) A model for the boreal summer intraseasonal oscillation. J Atmos Sci 54:72–86

Wang W, Saha S, Pan H-L (2004) Simulation and prediction of the MJO with the NCEP models. In: Proceedings of CMWF/CLIVAR workshop on simulation and prediction of intra-seasonal variability with emphasis on the MJO, Reading, United Kingdom, pp 237–249

Weickmann KM (1983) Intraseasonal circulation and outgoing longwave radiation modes during Northern Hemisphere winter. Mon Weather Rev 111:1838–1858

Woolnough SJ, Slingo JM, Hoskins BJ (2000) The relationship between convection and sea surface temperature on intraseasonal timescales. J Clim 13:2086–2104

Yansunari T (1979) Cloudiness fluctuations associated with the Northern Hemisphere monsoon. J Meteorol Soc Jpn 58:225–229

Zeng Y, Waliser DE, Stern WE, Jones C (2004) The role of coupled sea surface temperatures in the simulation of the tropical intraseasonal oscillation. J Clim 17:4109–4134